



Aggregation-Induced Emission by Molecular Design: A Route to High-Performance Light-Emitting Electrochemical Cells

Downloaded from: <https://research.chalmers.se>, 2025-12-04 23:33 UTC

Citation for the original published paper (version of record):

Tang, S., Wang, Z., Xu, Y. et al (2023). Aggregation-Induced Emission by Molecular Design: A Route to High-Performance Light-Emitting Electrochemical Cells. *Angewandte Chemie - International Edition*, 62(23).
<http://dx.doi.org/10.1002/anie.202302874>

N.B. When citing this work, cite the original published paper.

Organic Semiconductors

How to cite:

International Edition: doi.org/10.1002/anie.202302874

German Edition: doi.org/10.1002/ange.202302874

Aggregation-Induced Emission by Molecular Design: A Route to High-Performance Light-Emitting Electrochemical Cells

Shi Tang⁺, Zhi Wang⁺, Yanzi Xu, Huili Ma, Jia Wang, Christian Larsen, Dongfeng Dang,^{*} Ergang Wang,^{*} and Ludvig Edman^{*}

Abstract: The emission efficiency of organic semiconductors (OSCs) often suffers from aggregation caused quenching (ACQ). An elegant solution is aggregation-induced emission (AIE), which constitutes the design of the OSC so that its morphology inhibits quenching π - π interactions and non-radiative motional deactivation. The light-emitting electrochemical cell (LEC) can be sustainably fabricated, but its function depends on motion of bulky ions in proximity of the OSC. It is therefore questionable whether the AIE morphology can be retained during LEC operation. Here, we synthesize two structurally similar OSCs, which are distinguished by that **1** features ACQ while **2** delivers AIE. Interestingly, we find that the AIE-LEC significantly outperforms the ACQ-LEC. We rationalize our finding by showing that the AIE morphology remains intact during LEC operation, and that it can feature appropriately sized free-volume voids for facile ion transport and suppressed non-radiative excitonic deactivation.

Introduction

Many π -conjugated organic semiconductors (OSC) exhibit a strong propensity for a flat conformation, which renders for strong intermolecular interactions by π - π stacking in concentrated solution and in the solid state.^[1] This characteristic π - π stacking aggregation is attractive in that it enables for facile electronic transport,^[2] but it can unfortunately also result in a strong quenching of the emission capacity of the OSC through, e.g., the formation of dark or weakly emissive excimers.^[3] This frequently observed behavior is termed “aggregation caused quenching” (ACQ), and it is obviously a severe drawback for the utilization of OSCs in light-emission applications.^[3b,4]

In this context, the development of OSCs that are designed to efficiently inhibit this propensity for intermolecular π - π stacking aggregation, by the virtue of a twisted or rotated molecular conformation, is important.^[5] Moreover, it has proven possible to design such OSCs so that their molecular rotations and vibrations are strongly incapacitated in the solid state, which in turn suppresses the non-radiative deactivation of the excitons.^[6] Accordingly, the combination of these two features—the inhibition of intermolecular π - π stacking and the suppression of molecular rotations and vibrations—can result in that the efficiency of emission of these designed OSC actually *increases* during aggregation in the solid state; this phenomenon is therefore termed “aggregation induced emission” (AIE).^[7] It is possible to verify that an OSC emits with the process of AIE by the combined measurement of an increasing photoluminescence quantum yield (PLQY) and a prolongation of the radiative lifetime following the transfer of the OSC from dilute solution to the solid state.

OSCs that deliver AIE are obviously a good fit for the emitter in organic light-emitting diodes (OLEDs),^[8] since they, e.g., can eliminate the need for an additional host compound, and hence render for the attainment of high brightness at low voltage and resolve issues with phase separation.^[9] The light-emitting electrochemical cell (LEC) is a cost-efficient and sustainable alternative to the OLED,^[10] because its characteristic in situ electrochemical-doping mode enables for ambient-air printing and coating of the entire device stack using solely sustainable materials.^[11] However, the electrochemical-doping mode of LECs is directly dependent on the redistribution of bulky ions in close proximity of the emissive OSC in the active material, which opens up for the fundamental question as to whether

[*] Dr. S. Tang,⁺ Dr. J. Wang, Dr. C. Larsen, Prof. L. Edman
The Organic Photonics and Electronics Group, Department of Physics, Umeå University
90187 Umeå (Sweden)
E-mail: ludvig.edman@umu.se

Dr. Z. Wang,⁺ Y. Xu, Prof. D. Dang
School of Chemistry, Xi'an Key Laboratory of Sustainable Energy Material Chemistry, Xi'an Jiao Tong University
Xi'an 710049 (China)
E-mail: dongfengdang@xjtu.edu.cn

Dr. S. Tang,⁺ Dr. C. Larsen, Prof. L. Edman
LunaLEC AB
Linnaeus väg 24, 90187 Umeå (Sweden)

Prof. E. Wang
Department of Chemistry and Chemical Engineering/Applied Chemistry, Chalmers University of Technology
41296 Gothenburg (Sweden)
E-mail: ergang@chalmers.se

H. Ma
Key Laboratory of Flexible Electronics (KLOFE) & Institute of Advanced Materials (IAM), Nanjing Tech University (NanjingTech)
30 South Puzhu Road, Nanjing, 211816 (China)

[†] These authors contributed equally to this work.

© 2023 The Authors. Angewandte Chemie International Edition published by Wiley-VCH GmbH. This is an open access article under the terms of the Creative Commons Attribution License, which permits use, distribution and reproduction in any medium, provided the original work is properly cited.

the critical AIE morphology even can be retained during LEC operation?

In this context, we note that Park and Choe and co-workers^[12] reported on the synthesis of an ionic phenanthroimidazole:tetraphenylethylene small molecule that featured increasing emission efficiency in tetrahydrofuran (THF) solution with increasing addition of water, which is a commonly employed indicator of AIE behavior. They also introduced this emitter as the single-component active material in a two-electrode device, which delivered impressive blue electroluminescence. However, the time-dependent measurements that could have clarified whether ions are migrating in the active material during device operation were missing. The critical questions whether the AIE morphology can be retained during LEC operation, and whether this class of emitters is of practical interest for application in LEC devices, thus remain.

Here, we report on the designed synthesis of two structurally similar non-ionic donor-acceptor molecules, termed DA π AD-1 and DA π AD-2, with essentially identical emission properties in dilute solution, but which are distinguished by that DA π AD-1 features ACQ of the emission in neat solid form whereas DA π AD-2 exhibits AIE. We mixed each of the molecules separately with an ionic-liquid electrolyte, and employed these blends as the active material in two-electrode devices. We firmly establish that the ionic-liquid ions are migrating in both devices during the initial operation, and that they can enable for electrochemical p- and n-type doping of both DA π AD-1 and DA π AD-2. We find that the DA π AD-2 based LEC drastically outperforms the DA π AD-1 LEC by that it delivers much faster emission turn-on, higher emission efficiency, lower drive voltage, and better emission stability, and present complementary measurements that show that the enabler of the improved performance is the AIE morphology. We specifically find that an optimized AIE-LEC delivers intense near-infrared emission, with a peak radiance of 320 $\mu\text{W cm}^{-2}$ and a peak wavelength of 694 nm, during driving with a steady-state voltage of 4.3 V. Importantly, our study thus establishes that the AIE morphology can be retained during LEC operation, and that such appropriately designed AIE-LECs can deliver a highly promising emission performance.

Results and Discussion

Figures 1a,b present the molecular structure of the two OSCs: DA π AD-1 (a) and DA π AD-2 (b). The detailed description of their synthesis can be found in the Supporting Information, and key synthesis steps are displayed in Figure S1. In brief, a 4-(7-bromobenzo[c][1,2,5]thiadiazol-4-yl)-N,N-bis(4-methoxyphenyl)aniline precursor reacted chemically with either (4,4,9,9-tetrahexyl-4,9-dihydro-s-indaceno[5,1,2-b:5,6-b']dithiophene-2,7-diyl)bis(trimethylstannane) (DA π AD-1) or (4,4,9,9-tetrakis(4-hexylphenyl)-4,9-dihydro-s-indaceno[1,2-b:5,6-b']dithiophene-2,7-diyl)bis(trimethylstannane) (DA π AD-2) in a Stille-coupling reaction, using Pd(PPh₃)₄ as the catalyst. The molecular

structures were established and verified with a combination of ¹H NMR, ¹³C NMR and MALDI-TOF-MS (see Figures S2–S7) and the overall reaction product yield was $\approx 70\%$.

The two OSCs were designed with the same donor-acceptor- π -acceptor-donor (DA π AD) backbone structure, with triphenylamine (TPA) being the electron donor, benzothiadiazole (BT) the electron acceptor, and indaceno-dithiophene (IDT) being the central π bridging group. The four flexible hexyl side chains on the central part of the molecule were included for the attainment of high solubility in common hydrophobic solvents, such as toluene and THF. Importantly, DA π AD-2 is distinguished by that it features four “phenyl bridging units” (marked with blue background in Figure 1b) in between the central IDT group and the four hexyl side chains. Our first design goal with their introduction was to force a twisted molecular conformation of DA π AD-2, because of steric repulsion between the neighboring bulky phenyl groups, which in turn should inhibit the, for light-emission purposes, detrimental π - π stacking aggregation. Our second design goal was that the phenyl bridging units should function as intermolecular connection points in the solid state, which significantly restrict rotational and vibrational motions, and thereby slows down the non-radiative excitonic deactivation rate of DA π AD-2. Figures 1c,d present schematically our hypothesis for the contrasting stacking and intermolecular interactions of DA π AD-1 and DA π AD-2.

We performed calculations by density functional theory (DFT) to establish the single-molecule conformation and frontier orbitals of the two compounds, and to investigate the influence of the distinguishing phenyl bridging units on the single-molecule behavior of DA π AD-2. Figures 1e,f present the side-view and top-view conformation, which reveal that both OSCs feature a highly planar central acceptor- π -acceptor conformation (and a similar rotation at the peripheral TPA donor groups), but that the phenyl bridging units of DA π AD-2 adopt a strongly twisted conformation with respect to the planar central acceptor- π -acceptor group, with the calculated twisting angle being 76°. Figures 1g,h present the DFT-derived LUMO and HOMO distributions, and the associated energy levels. The two OSCs are essentially indistinguishable in both these aspects, with the HOMO being evenly delocalized over the entire molecule, while the LUMO is primarily localized on the two BT acceptor units. The calculated energy levels, with respect to the vacuum level, are -4.5 eV for the more delocalized HOMO and -2.4 eV for the LUMO; and the DFT calculated energy gap is accordingly 2.1 eV.

The aggregation properties and ordering capacity of the two OSCs in solid powder form were measured with X-ray diffraction (XRD) and differential scanning calorimetry (DSC). The two powders were prepared with an identical process, comprising slow evaporative drying of the purified synthesis solution. Figure 2a shows that the DA π AD-1 powder (solid black line) exhibits a complex XRD pattern with a large number of sharp peaks, which is indicative of a well-ordered crystalline sample. In contrast, the XRD pattern of the DA π AD-2 powder (dashed red line) is broad and featureless, which implies that DA π AD-2 is in a

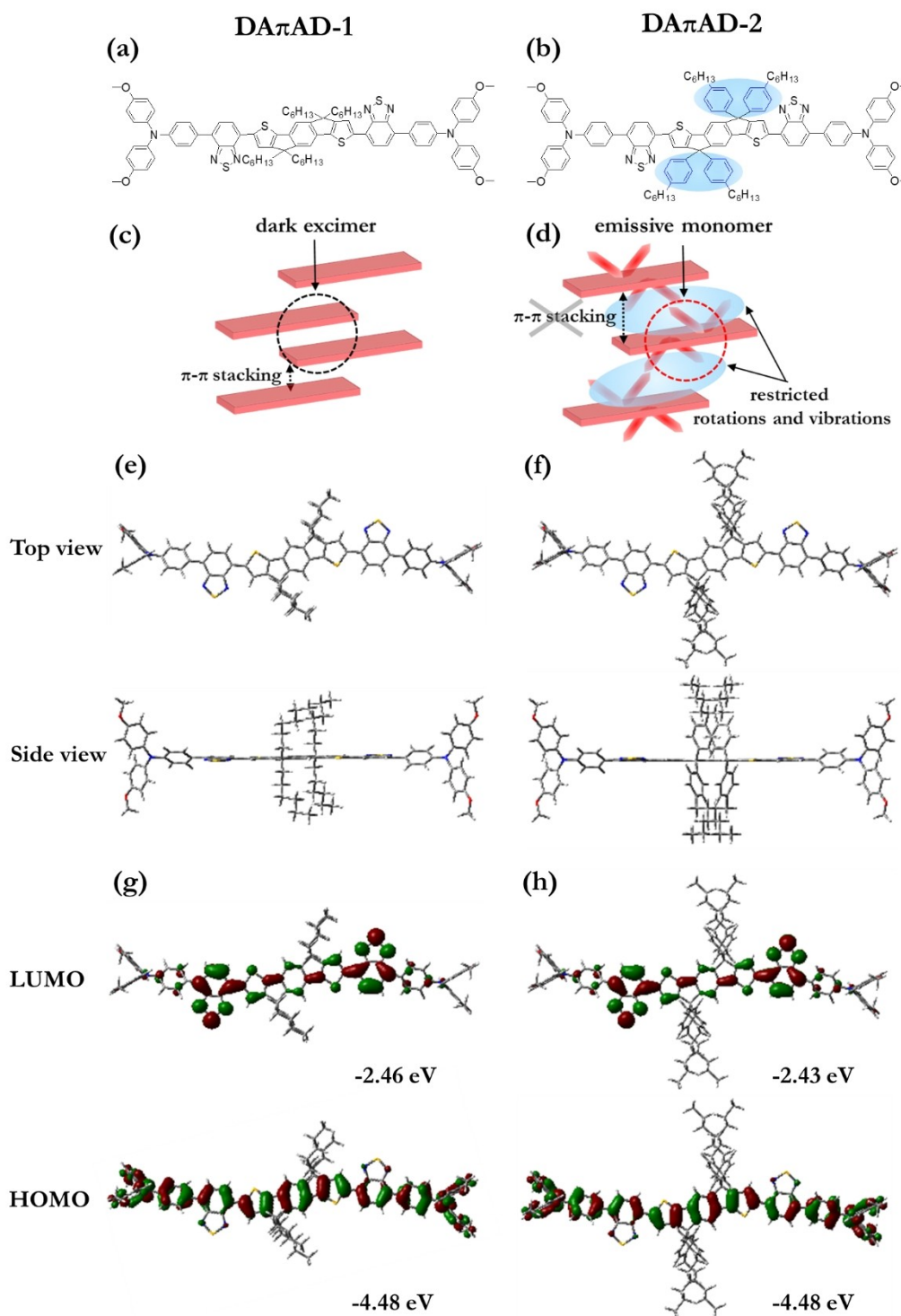


Figure 1. The molecular structure of a) DA π AD-1 and b) DA π AD-2, with the blue background identifying the distinguishing phenyl groups of DA π AD-2. c), d) Schematic illustrating our anticipated view of the distinguishing solid-state conformation and intermolecular stacking interactions as well as the primarily excited species. e), f) The DFT-derived optimum conformation in top view (upper panel) and side view (lower panel). g), h) The DFT-calculated frontier orbitals and the associated energy levels.

disordered amorphous state. Figure 2b present the DSC traces of the same pristine OSC powders recorded during the first heating cycle. DA π AD-1 (upper solid black line) exhibits a strong crystalline melting transition at $T_m=214^\circ\text{C}$,

whereas DA π AD-2 (lower dashed red line) solely features a glass transition with its onset at $T_g=123^\circ\text{C}$. These experimental results thus provide support for that the highly planar molecular conformation of DA π AD-1 facilitates for

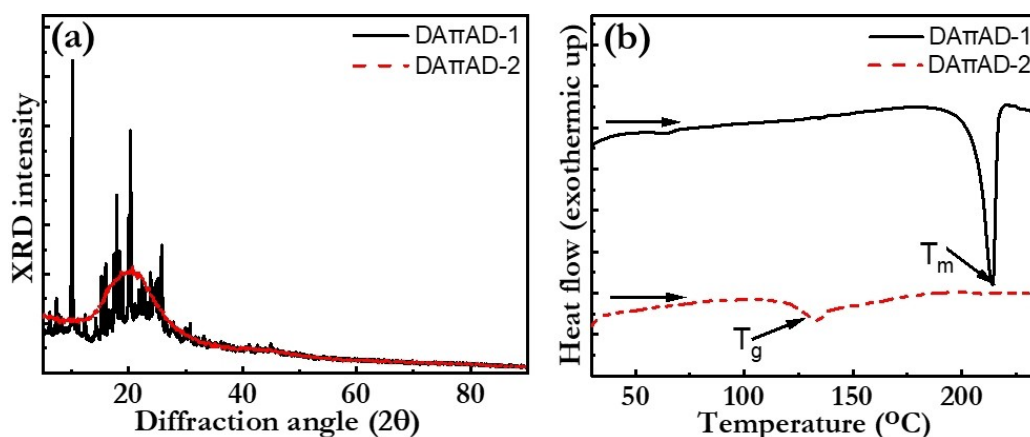


Figure 2. a) The measured X-ray diffraction spectrum of the two OSCs in powder form. b) The DSC traces of the two OSCs recorded during the first heating cycle, with the heating rate being $5^{\circ}\text{C min}^{-1}$. The melting and glass transitions are indicated, and the two traces are shifted in the vertical direction for clarity.

the formation of an ordered crystalline structure in the solid state. The more twisted conformation of DA π AD-2 instead inhibits such ordering and results in a solidification into a disordered amorphous glassy state. As such, these combined data support that DA π AD-1 can solidify into an ACQ conformation, whereas DA π AD-2 has a propensity for the formation of an AIE conformation, as schematically depicted in Figures 1c,d.

Figures 3a,b display the normalized absorption spectra of the two OSCs in dilute THF solution and as a spin-coated neat solid film, respectively. The two compounds exhibit very similar absorption behavior in both dilute solution and in solid form, and the difference between the two media is also quite minor. The broad absorption spectrum is divided into two bands, with the lower-energy band covering a majority of the visible regime while the higher-energy band is positioned in the UV range. The former is related to the HOMO–LUMO excitations depicted in Figures 1g,h, while the latter is attributed to a π – π^* transition within the IDT–BT part.^[13] The optical energy gap was derived from the measured absorption onset using the Tauc method (see Figure S8); in the dilute solution/neat film the optical energy gap is determined to be 2.02/1.93 eV for DA π AD-1 and 2.04/1.96 eV for DA π AD-2. The key optical properties are summarized in Table 1.

Figures 3c,d present the non-normalized PL spectra, with the corresponding values for the PLQY displayed in the lower inset. The two OSCs feature highly similar non-structured PL spectra, in both the dilute solution and in the neat thin film, with the broad PL peak positioned at ≈ 705 –710 nm and the full width at half maximum (FWHM) being

130 nm. The observed strong resemblance of both the absorption and the emission spectra for the two OSC implies that their optically active parts are essentially identical. This is in line with that the distinguishing phenyl bridging units (marked with blue background in Figure 1b) are physically separated from the optically active parts of the OSC molecules, i.e. the HOMO and LUMO distributions and the IDT–BT unit (see Figures 1g,h). Moreover, we find that the PL spectrum of a model TPA–BT donor-acceptor molecule (see Figure S9) is highly similar, which implies that the PL emission is primarily originating from the TPA–BT donor-acceptor part of DA π AD-1 and DA π AD-2.

However, the concentration dependence of the emission efficiency, as manifested in the PLQY, is drastically different. DA π AD-1 exhibits a significant drop in PLQY, from 35.8 to 1.6 %, when transferring from the dilute THF solution to the neat solid film. In contrast, the PLQY of DA π AD-2 increases, from 19.8 to 31.8 %, when the molecule is going from dilute solution to neat solid film. The photographs (recorded with identical exposure settings) in Figures 3c,d, left inset, of the UV-excited PL from the dilute solution and the neat thin film, respectively, provide visual evidence for this differing capacity for PL in the solid state.

Figures 3e,f present the temporal decay of the PL intensity (following optical excitation that ends at $t=0$ ns) for the dilute solution and the neat solid film, respectively. Three of the four measured PL transients were well fitted with a mono-exponential function and a constant background, with the exception being the DA π AD-1 neat film that required a bi-exponential function and a constant background for a good fit. This is in line with that this

Table 1: Summary of key measured optical and electronic properties of the two OSCs.

OSC	Absorption peak [nm]		PL _{peak} /PLQY [nm]/[%]		Radiative lifetime/ k_r/k_{nr} [ns]/[10^7 s^{-1}]		HOMO [eV]	LUMO [eV]
	Solution	Solid state	Solution	Solid state	Solution	Solid state		
DA π AD-1	564	573	703/35.8	709/1.6	2.66/13/24	0.56/3.5/214	-5.13	-3.15
DA π AD-2	559	564	703/19.8	703/31.8	2.09/9.5/28	3.61/8.8/1.9	-5.15	-3.15

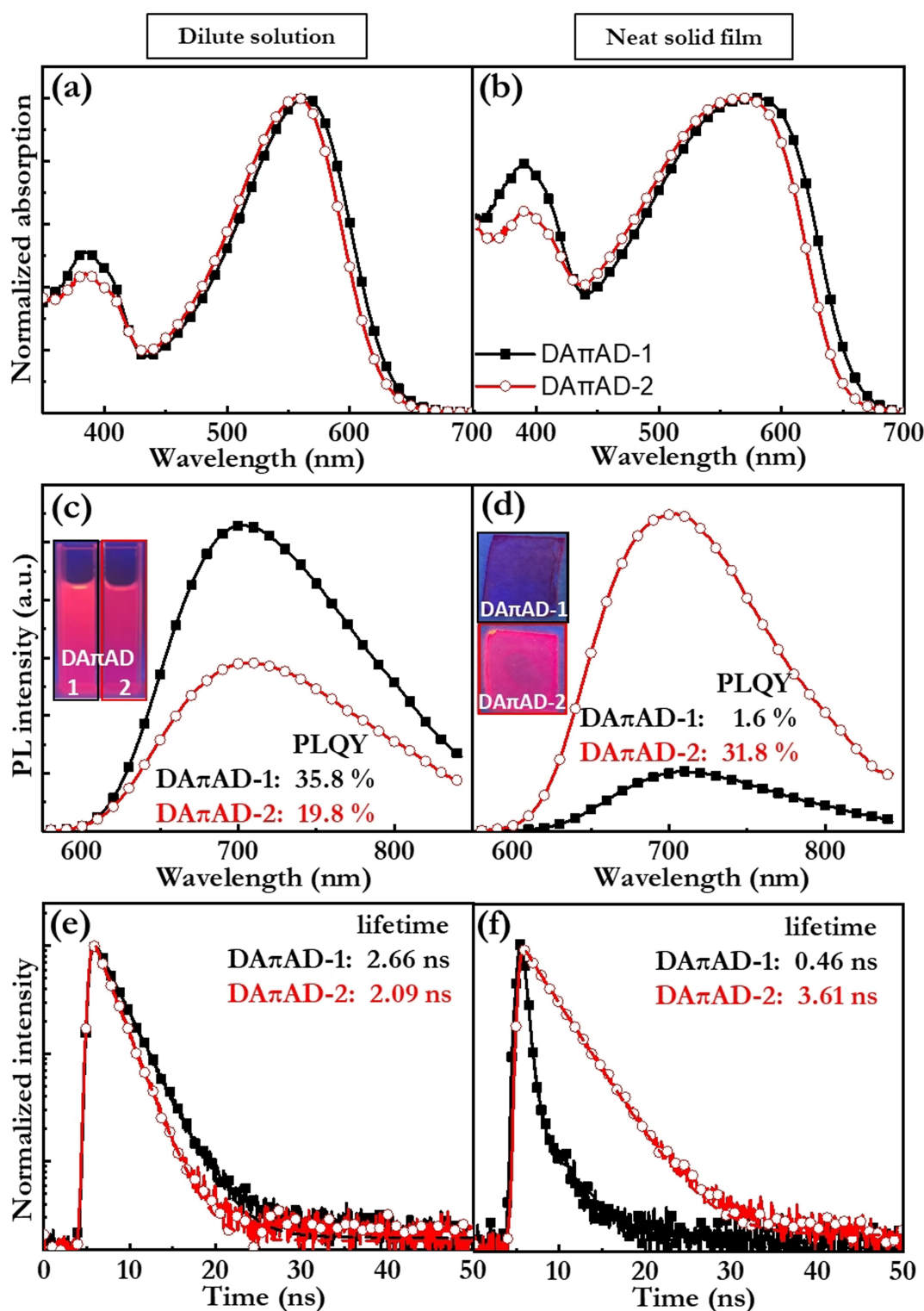


Figure 3. a), b) The normalized absorption spectra, c), d) the non-normalized PL spectra, and e), f) the PL intensity transients in dilute THF solution and as a solid neat film. The lower left inset in (b) identifies the OSC in all panels. The insets in (c), (d) are photographs of the PL from the dilute THF solution and the neat thin films, as recorded under exposure to UV illumination ($\lambda_{\text{peak}} = 365$ nm) in a dark room. The OSC concentration in the THF solution is ≈ 10 μM , and the film thickness was 120 nm.

system is distinguished by featuring significant π - π stacking interactions. The derived PL decay times are displayed in the upper right inset, while the calculated values for the

radiative and the non-radiative rate constants (k_r and k_{nr}) are presented in Table 1. (The decay time for the DA π AD-1 neat film is the average of the two exponentials.) The PL

decay time of DA π AD-1 drops markedly from 2.66 to 0.46 ns when going from dilute solution to neat film. In combination with the significant drop for the PLQY, this results in that the non-radiative decay rate k_{nr} of DA π AD-1 increases radically by a factor of eight during aggregation. In contrast, the PL decay time for DA π AD-2 is observed to increase from 2.09 to 3.61 ns when transferring from the dilute solution to the neat film, which results in that k_{nr} decreases by a factor of fifteen during aggregation. We have also investigated the effects on the PL of the addition of a polar non-solvent in the form of water to the dilute THF solution. Figure S10 shows that the initial addition of water results in a drop of the PL efficiency for both OSCs, and we speculate that this can be due to a transition to a poorly emissive molecular conformation. For larger amounts of added water, the response deviates between the two compounds, with the PL efficiency of DA π AD-1 decreasing markedly, whereas DA π AD-2 is rendered more emissive.

This combination of results confirms that the molecular design strategy has been successful, and that DA π AD-1 features ACQ, whereas DA π AD-2 can deliver AIE in the neat solid state. More specifically, the observed drop in the PLQY and the increase in the non-radiative decay rate with aggregation for DA π AD-1 are rationalized by that its molecular aggregation in the solid state is effectuated by intermolecular π - π interactions, and that the resulting ACQ morphology is concomitant with the formation of non-emissive low-energy species, such as excimers (see Figure 1c).^[3b] The contrasting increase in the PLQY and the decrease in the non-radiative rate for DA π AD-2 are instead explained by that its solid-state aggregation simultaneously prohibits intermolecular π - π interactions while rendering for the formation of other types of intermolecular bonds. The former process eliminates the formation of emission quenching species such as excimers, whereas the latter process suppresses non-radiative deactivation by freezing out rotations and vibrations (see Figure 1d).

We now turn our attention to the evaluation and application of the two OSCs as the electroactive and emissive species in a light-emitting electrochemical cell (LEC). The successful operation of an LEC is dependent on that injection-facilitating electric double layers (EDLs) first form at the electrode/active-material interfaces, and that the OSC thereafter can be electrochemically p-type doped at the positive anode and n-type doped at the negative cathode.^[14] More exactly, the injection of a hole/electron onto the OSC during the LEC initial turn-on phase is concomitant with the influx of an electrostatically compensating anion/cation in order to prevent the build-up of space charge, which in turn enables for high OSC conductivity. A convenient method to determine whether an OSC can allow for electrochemical doping is cyclic voltammetry (CV). Figure 4a presents a CV investigation of the two OSCs in neat solid film form. The observation of (partially) reversible oxidation and reduction events implies that both compounds exhibit capacity for the desired electrochemical p-type and n-type doping.

The HOMO/LUMO values of the OSCs can be derived from these CV data using the following Equation (1):

$$E_{\text{vacuum level}} = -e \cdot (4.8 \text{ V} + V_{\text{Fc/Fc}^+}) \quad (1)$$

where e is the elementary charge and $V_{\text{Fc/Fc}^+}$ is the onset potential for oxidation/reduction with respect to the Fc/Fc⁺ reference system, as identified by the vertical dashed lines in Figure 4a. This procedure delivers that the two OSCs feature essentially identical values for the HOMO and LUMO of -5.15 eV and -3.15 eV, respectively, which in turn yields that the electrochemical energy gap is 2.0 eV. We note that the latter is similar to the measured optical energy gap and the DFT calculated energy gap, but that the measured HOMO and LUMO levels from CV are lower than the calculated DFT values by 0.6 eV.

The position of the in situ formed emissive p-n junction in the active material has a strong influence on the LEC emission efficiency because of microcavity effects and because of varying proximity to quenching electrodes and polarons.^[15] It was recently demonstrated that the steady-state position of the p-n junction in LEC devices is determined by the electron-mobility/hole-mobility ratio, and it is therefore relevant to estimate this effective value by mobility measurements on single-carrier devices.^[16] Figure 4b presents the current density as a function of the voltage for (+)ITO/ZnO/OSC/Ca/Al(−) electron-only devices and (−)ITO/PEDOT:PSS/OSC/MoO₃/Au(+) hole-only devices. We find that the hole mobility is higher than the electron mobility for the two OSCs, which implies that the steady state p-n junction is positioned closer to the negative cathode in both the ACQ-LEC and the AIE-LEC. Moreover, we find that the two DA π AD-2 single-carrier devices feature a markedly higher current density (for both electrons and holes) than the corresponding DA π AD-1 devices, which implies that both the electron and the hole migrate faster in the AIE morphology.

The LEC active material was optimized to comprise a blend of the OSC and a tetrahexylammonium tetrafluoroborate (THABF₄) ionic-liquid electrolyte in a mass ratio of 1:0.05. Figure S11 shows that the PL spectra of the two active-material films are highly similar, and a comparison with the PL spectra of the neat OSC films in Figures 3c,d yields that the addition of the ionic-liquid electrolyte has a negligible influence on the shape of the PL spectrum. We further find that the addition of the electrolyte resulted in an increase of the PLQY from 1.6 % to a higher, but still modest, value of 3.9 % for DA π AD-1, and a slight increase from 31.8 to 33.1 % for DA π AD-2 (compare data in Table 2 with Table 1). The retained large PLQY difference between the two OSC films implies that the distinguishing ACQ and AIE morphologies of DA π AD-1 and DA π AD-2, respectively, are largely maintained following the addition of the ionic-liquid electrolyte.

The LEC devices were fabricated with an indium-tin-oxide/poly(3,4-ethylenedioxythiophene):poly(styrene sulfonate)/active-material/Al architecture, and driven by a constant current density of 74.5 mA cm^{−2}. We have investigated 4–8 devices in each category, with an observed variation in the presented performance metrics of less than 10 %. The presented data are for the champion devices.

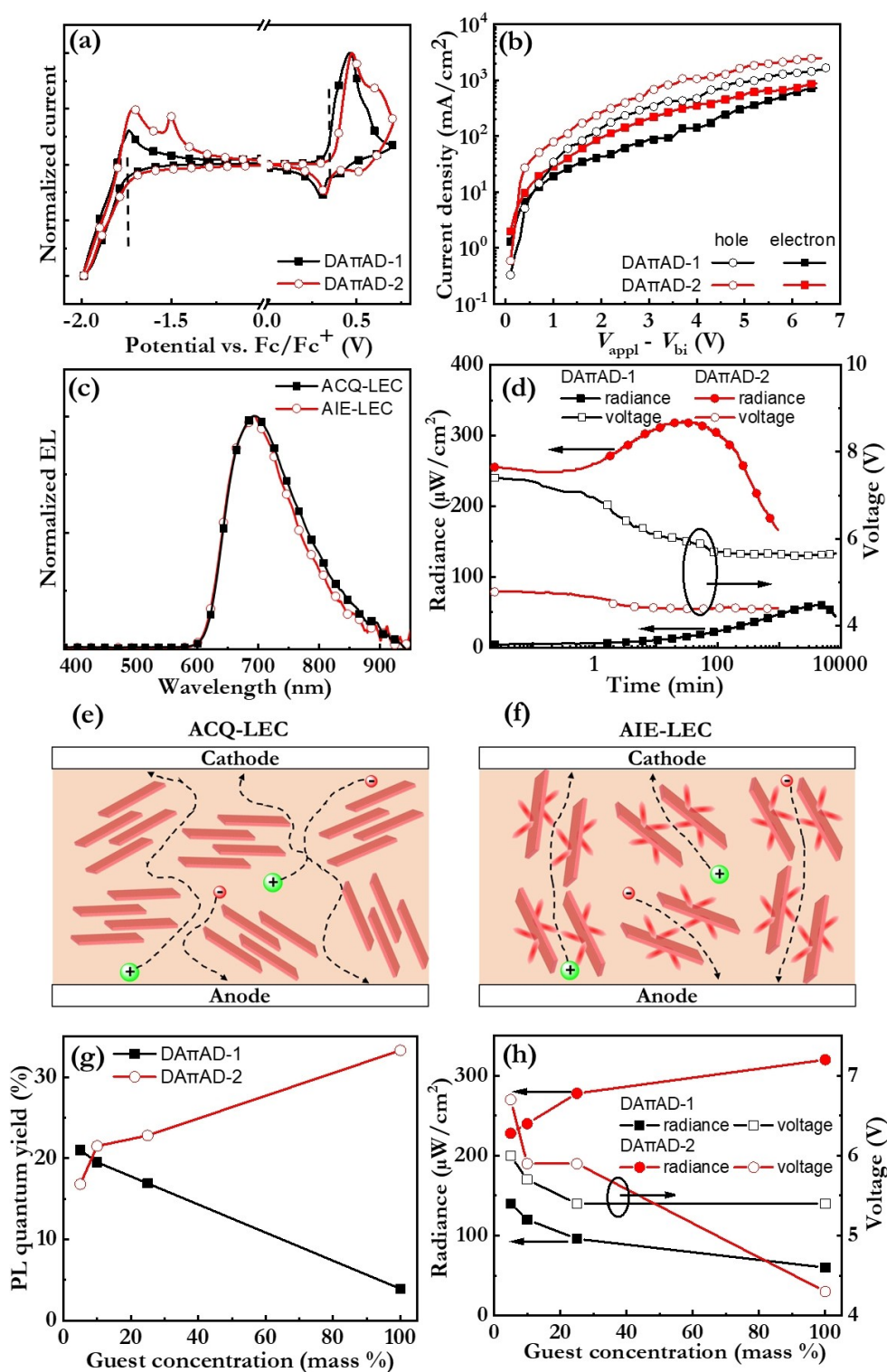


Figure 4. a) CV traces of the neat OSC thin films, as identified in the inset. The electrolyte was 0.1 M TBAPF₆ in CH₃CN and the scan rate was 0.1 V s⁻¹. b) The current density as a function of the voltage for (–)ITO/PEDOT:PSS/OSC/MoO₃/Au(+) hole-only devices (open symbols) and (+)ITO/ZnO/OSC/Ca/Al(–) electron-only devices (solid symbols), with the OSC in the active material identified in the inset. c) The normalized steady-state EL spectra of the two LEC devices. d) The temporal evolution of the radiance (left y-axis, solid symbols) and the voltage (right y-axis, open symbols) of two pristine LEC devices. The active-material thickness was 120 nm for all presented devices. Schematic illustration of the ion mobility pathways (dashed lines) in e) the AIE-LEC morphology and f) the ACQ-LEC morphology during the initial LEC operation. g) The PLQY of the blend-host:guest:electrolyte active material as a function of guest concentration. The blend-host mass ratio was 1:1, and the total concentration of the THABF₄ ionic-liquid electrolyte was 5 mass %. h) The peak radiance (left y-axis, solid symbols) and the minimum driving voltage (right y-axis, open symbols) for the blend-host:guest LECs as a function of guest concentration. All LECs were driven by a constant current density of 74.5 mA cm⁻².

Table 2: LEC performance recorded during constant-current driving by 74.5 mA cm^{-2} .

LEC	PL _{peak} /PLQY [nm]/[%] ^[a]	EL _{peak} [nm]	Turn-on time	Peak radiance [μW/cm ²]	EQE [%]	V _{min} [V]	High-radiance lifetime [h] ^[d]	Half lifetime [h] ^[e]
ACQ-LEC	712/3.9	695	1325 min ^[b]	60	0.048	5.4	0	100
AIE-LEC	706/33.3	694	2 s ^[c]	320	0.248	4.3	8.6	16

[a] active-material film. [b] time to radiance $> 50 \text{ μW cm}^{-2}$. [c] time to radiance $> 100 \text{ μW cm}^{-2}$. [d] time at radiance $> 200 \text{ μW cm}^{-2}$. [e] time to half peak radiance.

When the OSC in the active material is DA π AD-1/DA π AD-2, the device is termed as ACQ-LEC/AIE-LEC.

Figure 4c presents the steady-state EL spectra, and we find that both LECs feature a broad EL spectrum (FWHM = 130 nm) primarily located in the NIR range, with the peak emission positioned at EL_{peak} \approx 695 nm. We note that the EL peak is slightly blue shifted by \approx 10 nm compared to the PL peak of the active-material film (see Figure S11), the neat OSC film, and the dilute THF solution (see Table 1). Figure 4d shows the temporal evolution of the radiance (solid symbols) and the drive voltage (open symbols), respectively, of pristine LEC devices. (The fact that the primary LEC emission is outside the visible range motivated the measurement of radiance instead of luminance.) Both devices feature the LEC-characteristic increasing radiance and decreasing voltage during the initial constant-current operation, which is in line with that the two OSCs are in situ electrochemically p-type and n-type doped during the LEC operation. This conclusion is also in agreement with our analysis of the CV data in Figure 4a, and verifies that the ions can migrate into close proximity of the OSC in both the ACQ and AIE morphology.

Interestingly, Figure 4d shows that the AIE-LEC delivers a superior performance compared to the ACQ-LEC, since it turns on much faster ($< 2 \text{ s}$ to 100 μW cm^{-2} compared to $> 1300 \text{ min}$ to a lower radiance of 50 μW cm^{-2}), its peak radiance is notably higher ($320 \text{ vs. } 60 \text{ μW cm}^{-2}$), its minimum voltage is lower ($4.3 \text{ vs. } 5.4 \text{ V}$), and its operational lifetime at high radiance is significantly longer. We mention in passing that the attained NIR performance of the AIE-LEC is competitive with previously published NIR emitting LECs.^[17]

As described above, the in situ electrochemical doping during the initial LEC operation is effectuated by ion redistribution, which results in that the LEC turn-on time is determined by the ion mobility in the active material. The ion mobility is in turn depending on the existence of appropriately sized free volume sites, between which the ions can migrate.^[18] Thus, it is reasonable to conclude that the faster turn on of the AIE-LEC is due to that its active material features a superior nanomorphology from a free-volume perspective. We hypothesize that the inclusion of the distinguishing phenyl bridging groups in DA π AD-2 results in the formation of a large concentration of appropriately sized free-volume voids in between the backbone structures in the more open AIE morphology, whereas this formation is inhibited by the π - π stacking that is prominent in the more compact ACQ morphology, as depicted in the schematics in Figures 4e,f.

The more than five times higher values for the peak radiance and the EQE of the AIE-LEC is straightforward to attribute to the eight times higher thin-film PLQY for the AIE-based active material (see Table 1). The lower (minimum) voltage required to drive a set constant through the AIE-LEC does however mandate a more sophisticated analysis. At this point in time, the two EDLs are well developed, which render the electron and hole injection efficient and balanced. This implies that the difference in drive voltage is due to a difference in the effective bulk resistance of the active material. As each mobile ion in the active material can enable for one doping event,^[19] the fact that both devices comprise the same number of mobile ions in the active material yields that the (average) doping concentration at steady state (i.e. at minimum voltage) should be the same.

Since the active-material resistance is inversely dependent on the number of electronic charge carriers (i.e., the doping level) and their mobility, the conclusion that follows is that the AIE morphology features a higher effective electron and hole mobility than the ACQ morphology. This conclusion is in agreement with the single-carrier data presented in Figure 4b. We further find that the mobility-determining deviation in the morphology appears to be on the nanoscopic level, since both compounds form high-quality pinhole-free films on the microscopic level; see atomic force microscopy (AFM) images of the two thin films in Figure S12. We tentatively assign the higher electron and hole mobility of the AIE film morphology to that it exhibits a highly uniform “amorphous” nanostructure, whereas the strong propensity for stacking aggregations in the ACQ film results in the formation of nano-sized “grain boundaries” between the stacking regions that severely impede long-range electron and hole transport. It is finally reasonable that the significantly longer operational lifetime of the AIE-LEC can be attributed to its lower drive voltage, since a lowering of the voltage is an obvious mean to suppress detrimental electrochemical side reactions in LECs^[20] and other electrochemical devices.

It thus appears as though the superior performance of the AIE-LEC compared to the ACQ-LEC, at least in part, originates in the intimate AIE nanomorphology. A further test of the validity of this conclusion constitutes the dispersion of the OSCs as a minority component in a solid-state host matrix, so that the effects of the distinguishing ACQ and AIE morphologies are eliminated from the analysis. For this investigation, the two OSC were (in combination with the THABF₄ electrolyte) separately dispersed in a TCTA:POT2T solid-state blend-host matrix; see

Figure S13a for molecular structures. The blend-host mass ratio was 1:1, and the total concentration of the ionic-liquid electrolyte was 5 mass %. The electron-energy diagram of this blend-host suggests that it can form an intermolecular exciplex (Figure S13b), while the strong spectral overlap between the PL of the blend host and the absorption of the two guest compounds (Figure S13c) implies that the Förster resonance energy transfer from host to guest is efficient.

Figure 4g displays the dependency of the PLQY on the guest concentration in these two blend-host:guest:electrolyte active materials. Interestingly, the PLQY of the two active-material films converges to essentially the same value (of $\approx 20\%$) at a low guest concentration of 10 mass %, corresponding to a host concentration of 85 %, at which the distinguishing and characteristic guest ACQ/AIE morphology thus can be anticipated to be completely eliminated by dilution into the host.

Figure 4h presents the steady-state radiance (solid symbols) and voltage (open symbols) as a function of guest concentration for the two LEC devices based on these blend-host:guest active materials during constant-current driving. The corresponding spectral data, transients and overall performance are presented in Figure S14 and summarized in Table S1. We find that the difference in drive voltage is disappearing at lower guest concentration, which is expected considering that the (same) majority host is then the main charge transporter and that the trap depths are essentially the same.^[21] We also observe that the radiance (and therefore the EQE) is increasing with decreasing guest concentration for the DA π AD-1 based blend-host:guest LEC, whereas the opposite trend is exhibited by the LEC with DA π AD-2 as the guest emitter. We call attention to that this radiance behavior is qualitatively similar to the PLQY behavior in Figure 4g, which is in agreement with that the PLQY sets the ceiling for the attainable device performance. Importantly, the fact that the radiance at low guest concentration converges to essentially the same value for both blend-host:guest devices provides additional support for that it is indeed the morphology that it is the prime differentiator between the guest-only ACQ-LEC and AIE-LEC devices.

Conclusion

We employ and evaluate two highly similar OSCs for the electroactive species in LEC devices, which are distinguished by that one OSC emits by the conventional ACQ mechanism in the neat solid state whereas the other OSC features AIE. We find that the AIE morphology can be retained during LEC operation, and that the corresponding AIE-LEC delivers a significantly better performance than the ACQ-LEC in that it is notably faster to turn-on, more efficient and more stable. We specifically report on an AIE-LEC that turns on to bright emission within 2 s, delivers intense near-infrared emission with a peak radiance of $320 \mu\text{W cm}^{-2}$ and a peak wavelength of 694 nm, during long-term driving with a low voltage of 4.3 V. We rationalize our findings by showing that the distinguishing AIE morphology

features a strongly suppressed non-radiative deactivation of the excitons, a higher mobility for the electrons and holes, and a more appropriate distribution of free volume for facile ion transport. Our findings thus establish that the AIE-LEC concept is a promising route towards fast, efficient and low-voltage emissive devices, which can be fabricated with low-cost and sustainable methods.

Acknowledgements

The authors acknowledge generous financial support from Kempestiftelserna, the Swedish Research Council, the Swedish Energy Agency, the Swedish Foundation for Strategic Research, Wenner-Gren Foundations, Bertil & Britt Svenssons stiftelse för belysningsteknik, the National Natural Science Foundation of China (21975197), Shaanxi Province Key R&D Program-International Science and Technology Cooperation Project (2022KW-40), the Innovation Capability Support Program of Shaanxi (Program No. 2021TD-57), and the Wallenberg Initiative Materials Science for Sustainability (WISE) funded by the Knut and Alice Wallenberg Foundation.

Conflict of Interest

The authors declare no conflict of interest.

Data Availability Statement

The data that support the findings of this study are available from the corresponding author upon reasonable request.

Keywords: Aggregation Caused Quenching · Aggregation-Induced Emission · Electrochemical Doping · Light-Emitting Electrochemical Cell · Organic Semiconductor

- [1] a) P. Maria, S. Griggs, R. B. Rashid, B. D. Paulsen, J. Surgailis, K. Thorley, V. N. Le, G. T. Harrison, C. Combe, R. Hallani, A. Giovannitti, A. F. Paterson, S. Inal, J. Rivnay, I. McCulloch, *Chem. Mater.* **2022**, *34*, 8593–8602; b) A. Minotto, I. Bulut, A. G. Rapisdis, G. Carnicella, M. Patrini, E. Lunedei, H. L. Anderson, F. Cacialli, *Light: Sci. Appl.* **2021**, *10*, 18.
- [2] a) G. C. Solomon, C. Herrmann, J. Vura-Weis, M. R. Wasielewski, M. A. Ratner, *J. Am. Chem. Soc.* **2010**, *132*, 7887–7889; b) W. T. Geng, M. Oda, J. Nara, H. Kondo, T. Ohno, *J. Phys. Chem. B* **2008**, *112*, 2795–2800; c) S. T. Schneebeli, M. Kamenetska, Z. Cheng, R. Skouta, R. A. Friesner, L. Venkataraman, R. Breslow, *J. Am. Chem. Soc.* **2011**, *133*, 2136–2139.
- [3] a) G. V. Büna, *Ber. Bunsen-Ges.* **1970**, *74*, 1294–1295; b) S. A. Jenekhe, J. A. Osaheni, *Science* **1994**, *265*, 765–768.
- [4] a) R. H. Friend, R. W. Gymer, A. B. Holmes, J. H. Burroughes, R. N. Marks, C. Taliani, D. D. C. Bradley, D. A. D. Santos, J. L. Brédas, M. Lögdlund, W. R. Salaneck, *Nature* **1999**, *397*, 121–128; b) J. Cornil, D. A. dos Santos, X. Crispin, R. Silbey, J. L. Brédas, *J. Am. Chem. Soc.* **1998**, *120*, 1289–1299.

- [5] a) K.-T. Wong, Y.-Y. Chien, R.-T. Chen, C.-F. Wang, Y.-T. Lin, H.-H. Chiang, P.-Y. Hsieh, C.-C. Wu, C. H. Chou, Y. O. Su, G.-H. Lee, S.-M. Peng, *J. Am. Chem. Soc.* **2002**, *124*, 11576–11577; b) H. J. Cho, S. W. Kim, S. Kim, S. Lee, J. Lee, Y. Cho, Y. Lee, T.-W. Lee, H.-J. Shin, C. Song, *J. Mater. Chem. C* **2020**, *8*, 17289–17296.
- [6] a) D. G. Congrave, B. H. Drummond, V. Gray, A. D. Bond, A. Rao, R. H. Friend, H. Bronstein, *Polym. Chem.* **2021**, *12*, 1830–1836; b) J. Royakkers, K. Guo, D. T. W. Toolan, L.-W. Feng, A. Minotto, D. G. Congrave, M. Danowska, W. Zeng, A. D. Bond, M. Al-Hashimi, T. J. Marks, A. Facchetti, F. Cacialli, H. Bronstein, *Angew. Chem. Int. Ed.* **2021**, *60*, 25005–25012.
- [7] a) J. Luo, Z. Xie, J. W. Y. Lam, L. Cheng, H. Chen, C. Qiu, H. S. Kwok, X. Zhan, Y. Liu, D. Zhu, B. Z. Tang, *Chem. Commun.* **2001**, 1740–1741; b) Y. Hong, J. W. Y. Lam, B. Z. Tang, *Chem. Soc. Rev.* **2011**, *40*, 5361–5388; c) Z. Zhao, H. Zhang, J. W. Y. Lam, B. Z. Tang, *Angew. Chem. Int. Ed.* **2020**, *59*, 9888–9907; d) X. Cai, B. Liu, *Angew. Chem. Int. Ed.* **2020**, *59*, 9868–9886; e) F. Würthner, *Angew. Chem. Int. Ed.* **2020**, *59*, 14192–14196.
- [8] a) H. Chen, H. Liu, Y. Xiong, J. He, Z. Zhao, B. Z. Tang, *Mater. Chem. Front.* **2022**, *6*, 924–932; b) H. J. Kim, H. Kang, J.-E. Jeong, S. H. Park, C. W. Koh, C. W. Kim, H. Y. Woo, M. J. Cho, S. Park, D. H. Choi, *Adv. Funct. Mater.* **2021**, *31*, 2102588; c) J. Guo, J. Fan, L. Lin, J. Zeng, H. Liu, C.-K. Wang, Z. Zhao, B. Z. Tang, *Adv. Sci.* **2019**, *6*, 1801629; d) H. Liu, H. Liu, J. Fan, J. Guo, J. Zeng, F. Qiu, Z. Zhao, B. Z. Tang, *Adv. Opt. Mater.* **2020**, *8*, 2001027; e) H. Chen, H. Liu, P. Shen, J. Zeng, R. Jiang, Y. Fu, Z. Zhao, B. Z. Tang, *Adv. Opt. Mater.* **2021**, *9*, 2002019; f) J. Chen, J. Zeng, X. Zhu, J. Guo, Z. Zhao, B. Z. Tang, *CCS Chem.* **2021**, *3*, 230–240; g) F. Ma, X. Zhao, H. Ji, D. Zhang, K. Hasrat, Z. Qi, *J. Mater. Chem. C* **2020**, *8*, 12272–12283; h) X. Wang, S. Wang, J. Lv, S. Shao, L. Wang, X. Jing, F. Wang, *Chem. Sci.* **2019**, *10*, 2915–2923; i) J. Guo, X.-L. Li, H. Nie, W. Luo, S. Gan, S. Hu, R. Hu, A. Qin, Z. Zhao, S.-J. Su, B. Z. Tang, *Adv. Funct. Mater.* **2017**, *27*, 1606458.
- [9] a) J. Zeng, J. Guo, H. Liu, J. W. Y. Lam, Z. Zhao, S. Chen, B. Z. Tang, *Chem. Asian J.* **2019**, *14*, 828–835; b) Y. Fu, H. Liu, X. Zhu, J. Zeng, Z. Zhao, B. Z. Tang, *J. Mater. Chem. C* **2020**, *8*, 9549–9557; c) D. Ma, *Top. Curr. Chem.* **2021**, *379*, 16; d) Y.-F. Shen, M. Li, W.-L. Zhao, Y.-F. Wang, H.-Y. Lu, C.-F. Chen, *Mater. Chem. Front.* **2021**, *5*, 834–842; e) H. Liu, J. Zeng, J. Guo, H. Nie, Z. Zhao, B. Z. Tang, *Angew. Chem. Int. Ed.* **2018**, *57*, 9290–9294; f) C. Wu, C. Shi, Y. Zheng, J. Zhang, Y. Wang, N. Sun, Q. Wang, Z.-H. Lu, *Chem. Eng. J.* **2022**, *431*, 133249; g) R. Furue, T. Nishimoto, I. S. Park, J. Lee, T. Yasuda, *Angew. Chem. Int. Ed.* **2016**, *55*, 7171–7175; h) H. J. Kim, S. K. Kim, M. Godumala, J. Yoon, C. Y. Kim, J.-E. Jeong, H. Y. Woo, J. H. Kwon, M. J. Cho, D. H. Choi, *Chem. Commun.* **2019**, *55*, 9475–9478.
- [10] a) Q. Pei, G. Yu, C. Zhang, Y. Yang, A. J. Heeger, *Science* **1995**, *269*, 1086–1088; b) A. Sandström, L. Edman, *Energy Technol.* **2015**, *3*, 329–339; c) S. Tang, L. Edman, *Top. Curr. Chem.* **2016**, *374*, 40; d) J. D. Slinker, J. Rivnay, J. S. Moskowitz, J. B. Parker, S. Bernhard, H. D. Abruna, G. G. Malliaras, *J. Mater. Chem.* **2007**, *17*, 2976–2988.
- [11] a) A. Sandström, H. F. Dam, F. C. Krebs, L. Edman, *Nat. Commun.* **2012**, *3*, 1002; b) A. Sandström, A. Asadpoordarvish, J. Enevold, L. Edman, *Adv. Mater.* **2014**, *26*, 4975–4980; c) A. Asadpoordarvish, A. Sandström, C. Larsen, R. Bollström, M. Toivakka, R. Österbacka, L. Edman, *Adv. Funct. Mater.* **2015**, *25*, 3238–3245; d) Z. Zhang, K. Guo, Y. Li, X. Li, G. Guan, H. Li, Y. Luo, F. Zhao, Q. Zhang, B. Wei, Q. Pei, H. Peng, *Nat. Photonics* **2015**, *9*, 233–238; e) K. Sato, S. Uchida, S. Toriyama, S. Nishimura, K. Oyaizu, H. Nishide, Y. Nishikitani, *Adv. Mater. Technol.* **2017**, *2*, 1600293; f) J. Zimmermann, L. Porcarelli, T. Rödlmeier, A. Sanchez-Sanchez, D. Mecerreyes, G. Hernandez-Sosa, *Adv. Funct. Mater.* **2018**, *28*, 1705795; g) S. Arumugam, Y. Li, J. E. Pearce, K. L. Court, G. Piana, E. H. Jackman, O. J. Ward, M. D. B. Charlton, J. Tudor, D. C. Harrowven, S. P. Beeby, *Org. Electron.* **2022**, *105*, 106513; h) R. D. Costa, D. Tordera, E. Orti, H. J. Bolink, J. Schönlé, S. Graber, C. E. Housecroft, E. C. Constable, J. A. Zampese, *J. Mater. Chem.* **2011**, *21*, 16108–16118; i) L. Mardegan, A. Paliwal, K. P. S. Zanon, D. Tordera, H. J. Bolink, *Adv. Opt. Mater.* **2022**, *10*, 2201953; j) N. Jürgensen, J. Zimmermann, A. J. Morfa, G. Hernandez-Sosa, *Sci. Rep.* **2016**, *6*, 36643; k) J. Zimmermann, N. Jürgensen, A. J. Morfa, B. Wang, S. Tekoglu, G. Hernandez-Sosa, *ACS Sustainable Chem. Eng.* **2016**, *4*, 7050–7055; l) Y. Liu, S. Tang, X. Wu, N. Boulanger, E. Gracia-Espino, T. Wågberg, L. Edman, J. Wang, *Nano Res.* **2022**, *15*, 5610–5618.
- [12] J. Park, K. Shanmugasundaram, J. C. John, Y. Choe, *J. Photochem. Photobiol. A* **2019**, *374*, 10–15.
- [13] R. S. Ashraf, B. C. Schroeder, H. A. Bronstein, Z. Huang, S. Thomas, R. J. Kline, C. J. Brabec, P. Rannou, T. D. Anthopoulos, J. R. Durrant, I. McCulloch, *Adv. Mater.* **2013**, *25*, 2029–2034.
- [14] P. Matyba, K. Maturova, M. Kemerink, N. D. Robinson, L. Edman, *Nat. Mater.* **2009**, *8*, 672.
- [15] a) E. M. Lindh, P. Lundberg, T. Lanz, L. Edman, *Sci. Rep.* **2019**, *9*, 10433; b) E. M. Lindh, P. Lundberg, T. Lanz, J. Mindemark, L. Edman, *Sci. Rep.* **2018**, *8*, 6970; c) H.-C. Su, *ChemPlusChem* **2018**, *83*, 197–210; d) T. W. Wang, H. C. Su, *Org. Electron.* **2013**, *14*, 2269–2277.
- [16] a) J. Ràfols-Ribé, X. Zhang, C. Larsen, P. Lundberg, E. M. Lindh, C. T. Mai, J. Mindemark, E. Gracia-Espino, L. Edman, *Adv. Mater.* **2022**, *34*, 2107849; b) M. Diethelm, A. Deviš, W.-H. Hu, T. Zhang, R. Furrer, C. Vael, S. Jenatsch, F. Nüesch, R. Hany, *Adv. Funct. Mater.* **2022**, *32*, 2203643.
- [17] a) A. Pertegás, D. Tordera, J. J. Serrano-Pérez, E. Orti, H. J. Bolink, *J. Am. Chem. Soc.* **2013**, *135*, 18008–18011; b) B. Pashaei, S. Karimi, H. Shahroosvand, M. Pilkington, *Adv. Funct. Mater.* **2020**, *30*, 1908103; c) E. Fresta, A. Charisiadis, L. M. Cavinato, N. Palandjian, K. Karikis, V. Nikolaou, G. Charalambidis, A. G. Coutsolelos, R. D. Costa, *Adv. Photonics Res.* **2021**, *2*, 2000188; d) C.-C. Ho, H.-F. Chen, Y.-C. Ho, C.-T. Liao, H.-C. Su, K.-T. Wong, *Phys. Chem. Chem. Phys.* **2011**, *13*, 17729–17736; e) C.-L. Lee, C.-Y. Cheng, H.-C. Su, *Org. Electron.* **2014**, *15*, 711–720; f) G.-Y. Chen, B.-R. Chang, T.-A. Shih, C.-H. Lin, C.-L. Lo, Y.-Z. Chen, Y.-X. Liu, Y.-R. Li, J.-T. Guo, C.-W. Lu, Z.-P. Yang, H.-C. Su, *Chem. Eur. J.* **2019**, *25*, 5489–5497; g) B. N. Bideh, H. Shahroosvand, *Sci. Rep.* **2017**, *7*, 7.
- [18] J. Mindemark, L. Edman, *J. Mater. Chem. C* **2016**, *4*, 420–432.
- [19] J. Fang, Y. Yang, L. Edman, *Appl. Phys. Lett.* **2008**, *93*, 063503.
- [20] J. Fang, P. Matyba, N. D. Robinson, L. Edman, *J. Am. Chem. Soc.* **2008**, *130*, 4562–4568.
- [21] S. Tang, A. Sandström, P. Lundberg, T. Lanz, C. Larsen, S. Van Reenen, M. Kemerink, L. Edman, *Nat. Commun.* **2017**, *8*, 1190.

Manuscript received: February 25, 2023

Accepted manuscript online: March 30, 2023

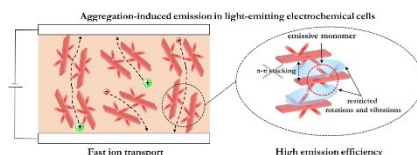
Version of record online: ■■■■■

Research Articles

Organic Semiconductors

S. Tang, Z. Wang, Y. Xu, H. Ma, J. Wang,
C. Larsen, D. Dang,* E. Wang,*
L. Edman* **e202302874**

Aggregation-Induced Emission by Molecular Design: A Route to High-Performance Light-Emitting Electrochemical Cells



The solid-state nanomorphology that enables aggregation-induced emission (AIE) is shown to be compatible with the ion redistribution that defines the operation of light-emitting electrochemical cells (LECs), and appropriately designed AIE-LECs are reported to deliver fast-to-turn and efficient emission at low voltage.